

X-Ray Observations of the Supernova Remnant W 28 with Suzaku — I. Spectral Study of the Recombining Plasma

Makoto SAWADA and Katsuji KOYAMA

*Department of Physics, Graduate School of Science, Kyoto University, Kitashirakawa Oiwake-cho, Sakyo-ku, Kyoto 606-8502
sawada@cr.scphys.kyoto-u.ac.jp*

(Received 2011 November 29; accepted 2012 February 4)

Abstract

We present the Suzaku results of the mixed-morphology supernova remnant W 28. The X-ray spectra of the central region of W 28 exhibit many bright emission lines from highly ionized atoms. An optically thin thermal plasma in collisional ionization equilibrium, either of single-temperature or multi-temperature failed to reproduce the data with line-like and bump-like residuals at the Si Lyman α energy and at 2.4–5.0 keV, respectively. The bumps probably correspond to radiative recombination continua from He-like Si and S. A simple recombining plasma model nicely fit the bump structures, but failed to fit low energy bands. The overall spectra can be fit with a multi-ionization temperature plasma with a common electron temperature. The multi-ionization temperatures are interpreted as elemental difference of ionization and recombination timescales. These results prefer the rarefaction scenario for the origin of the recombining plasma.

Key words: ISM: individual (W 28)—ISM: supernova remnants—X-ray:ISM

1. Introduction

The evolution of thermal plasmas in supernova remnants (SNRs) is a dynamical time-sequence of shock-heated gas. At first, a large fraction of the expanding velocity is converted to random velocity (thermal energy). The shock-heated temperature is proportional to the mass of the plasma particles (electrons and ions); the ion temperature is more than 1000 times higher than the electron temperature (hereafter, T_e). Subsequently, the energy of ions is transferred to the electrons, and hence T_e gradually increases. Then the high temperature electrons slowly ionize the ions to higher ionization states. Here we define the ionization temperature (T_z) as a parameter to represent populations of ionization states; T_z is equal to the plasma temperature in collisional ionization equilibrium (CIE), which realizes the observed populations of ionization states.

The typical timescale of ionization in SNR plasmas (density is $\sim 1 \text{ cm}^{-3}$) is $\sim 10^{12-13} \text{ s}$ (Smith & Hughes 2010). Accordingly, most of the young-intermediate SNRs have lower T_z than T_e , which is called an under-ionized or ionizing plasma, because ionization dominates over recombination. In fact, young-middle-aged shell-like SNRs have been generally described with an ionizing plasma model (e.g. Kinugasa & Tsunemi 1999).

Recently, Suzaku has discovered strong radiative recombination continua (RRCs) in the X-ray spectra of three SNRs, IC 443, W49B, and G 359.1–0.5 (Yamaguchi et al. 2009; Ozawa et al. 2009; Ohnishi et al. 2011). The strong RRCs appear when recombination dominates over ionization (recombining plasma). In fact, the X-ray spectra of these SNRs can be fit by neither CIE plasma, ionizing plasma, nor any combination of them. Detailed spectro-

scopic analysis with the recombining plasma code revealed that T_z are 1.5–3 times higher than T_e . These SNRs have some common features. (1) All are categorized into mixed-morphology SNRs (MM SNRs: Rho & Petre 1998), which have a radio shell with centrally-filled thermal X-rays. (2) These are associated with shocked molecular clouds and GeV/TeV γ -ray emissions (e.g. Yusef-Zadeh et al. 2003a; Abdo et al. 2010a).

W 28 (G 6.4–0.1), a bright MM SNR, exhibits above two conditions; a shock interaction with the ambient gas indicated by the expanding H I shell (Velázquez et al. 2002), broad CO, CS, and H₂ emission lines (Arikawa et al. 1999; Reach et al. 2005), and OH (1720 MHz) masers (Yusef-Zadeh et al. 2003b). Also GeV and TeV γ -rays were detected (Abdo et al. 2010b; Aharonian et al. 2008).

From the estimated distance of $1.9 \pm 0.3 \text{ kpc}$ (Velázquez et al. 2002), the angular size of $\sim 50'$ is $\sim 30 \text{ pc}$. The large size, possible association to the nearby pulsar (Kaspi et al. 1993), and dynamical evolution of the H I shell (Velázquez et al. 2002) constrain the age of W 28 to be 33,000–150,000 yr.

ROSAT and ASCA mapped the entire remnant in the X-ray band (Rho & Borkowski 2002) and found center-filled structure with partial shells at northeast and southwest. The X-ray spectrum in the central region had hard X-ray emissions up to $\sim 7 \text{ keV}$ with the iron (Fe) $K\alpha$ line, and was fit with a two-temperature plasma of 0.67 keV and 1.8 keV in CIE or ionizing. Thus no hint of recombining plasma has been reported from W 28, although this SNR shares the common features with the three SNRs of recombining plasmas. The aim of this paper is to search for and quantitatively study recombining plasmas with the superior energy resolution and the large effective area of the X-ray Imaging Spectrometer (XIS: Koyama et al.

Table 1. Log of Suzaku observations of W 28.

Sequence no.	Aim point		Start date	Effective exposure	Field name
	α (J2000.0)	δ (J2000.0)			
505005010	18 ^h 00 ^m 17 ^s	−23°21′59″	2010/04/03	73.0 ks	Center
500008010	18 ^h 03 ^m 49 ^s	−22°01′03″	2006/04/07	40.7 ks	Nearby sky

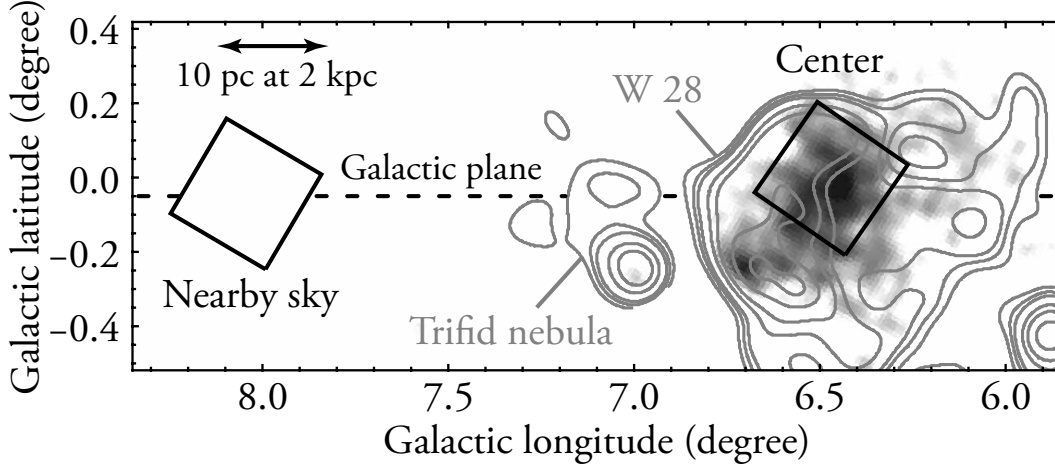


Fig. 1. Wide-field X-ray image retrieved from the ROSAT All Sky Survey in grayscale (Snowden et al. 1995). Overlaid contours are the radio continuum map at 1.4 GHz by the Very Large Array (Dubner et al. 2000). The XIS FOVs are shown with the solid squares.

2007) onboard Suzaku (Mitsuda et al. 2007). Throughout this paper, the distance of 2 kpc is adopted and statistical errors are at the 90% confidence level.

2. Observations and Data Reductions

We observed the central bright region of W 28 with the XIS as a part of the recombining plasma survey project (PI: Koyama, K.). The local background was obtained from the Suzaku archive near W 28. The locations of the two fields and the observation log are respectively shown in figure 1 and in table 1.

The XIS consists of four CCD cameras each placed at the focal planes of four X-Ray Telescopes (XRTs: Serlemitsos et al. 2007). Three sensors employ Front-Illuminated (FI) CCDs (XIS 0, 2, and 3), while the other employs a Back-Illuminated (BI) CCD (XIS 1). The entire region of XIS 2 and one of the edge region of XIS 0 have not been functional since anomalies in 2006 November and in 2009 June, respectively. The field of view (FOV) of the XIS combined with XRT covers a $18' \times 18'$ region with the pixel scale of $1'' \text{ pixel}^{-1}$. The angular resolution of $1.9\text{--}2.3$ in the half-power diameter is almost independent of photon energies and off-axis angles within $\sim 10\%$. The total effective area of the operational XIS 0, 1, and 3 combined with the three XRTs is 1070 cm^2 at 1.5 keV. Due to the low orbital altitude of Suzaku at $\sim 550 \text{ km}$, the XIS achieves a low and stable background environment.

The XIS observation was made with the normal clocking mode. The software package HEASoft version 6.11 and

the pipeline processing version 2.4 were used for the data reduction. To restore the radiation-induced degradation in the energy gain and resolution, the spaced-row charge injection technique (SCI: Bautz et al. 2004) was applied with the makepi files version 20110621 provided by the XIS team (Uchiyama et al. 2009). Then the systematic uncertainty in the energy scale is $\lesssim 10 \text{ eV}$ at 5.9 keV. We removed hot and flickering pixels, and events during the South Atlantic Anomaly passages and in the Earth night-time and day-time elevation angles below 5° and 20° , respectively.

3. Analyses and Results

3.1. Background Estimation

Figure 2 shows the X-ray images of the W 28 center and the nearby-sky fields. The non-X-ray background (NXB) generated by xisnxbgen (Tawa et al. 2008) was subtracted, and then the vignetting and exposure corrections were made.

We can see excess emission from W 28 in the soft X-ray band, but no excess in the hard band (figure 2). We extracted the source and background spectra from the solid and dashed circles in figure 2, respectively. The results are shown in figure 3, where the effective area of the background is normalized to that of the source region.

Compared with the background, the source spectrum shows obvious excess below $\sim 5 \text{ keV}$ but no excess in the hard X-ray band $\gtrsim 5 \text{ keV}$ (figure 3), consistent with the images. This result is, however, inconsistent with the pre-

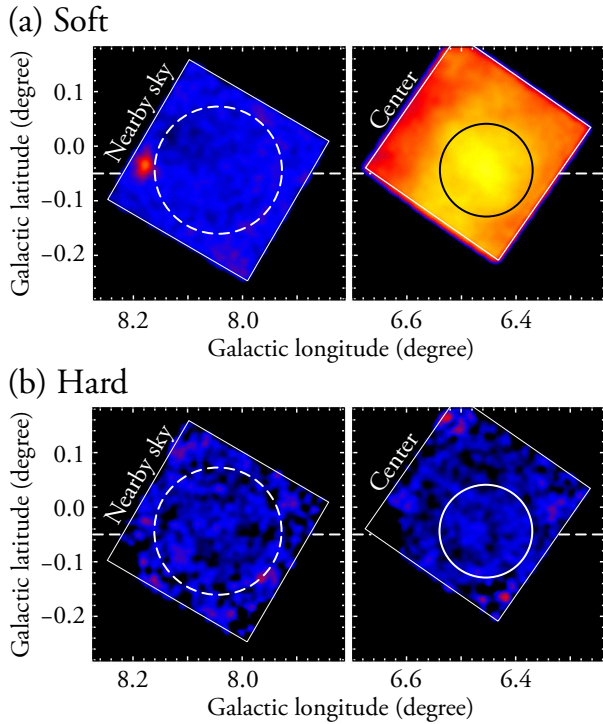


Fig. 2. Band-limited images with the XIS: (a) soft X-rays in 0.5–5.0 keV and (b) hard X-rays in 5.0–8.0 keV. The data with the three CCDs were merged. The NXB was subtracted and then the exposure and vignetting effects were corrected. The source and background extraction regions are shown in the solid and dashed circles, respectively.

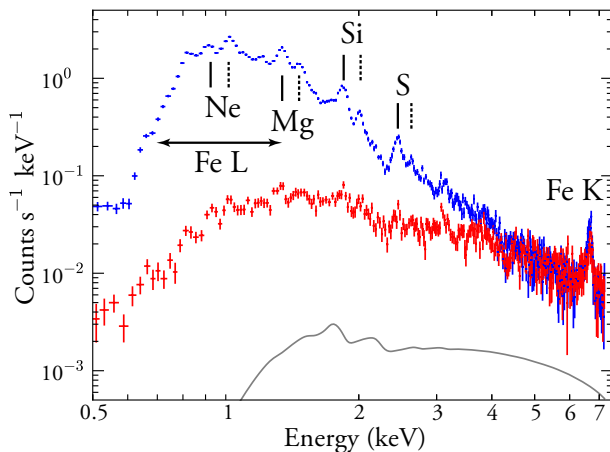


Fig. 3. Comparison of the source (blue) and the normalized background (red) spectra. For visibility, only merged spectra of FI (XIS 0 and XIS 3) are displayed. The solid and dashed black lines show the center energies of the K α lines from He-like and H-like ions, respectively. The gray line indicates the CXB spectrum.

vious ASCA observations, which claimed the detection of hard X-ray emission up to ~ 7 keV with the Fe K α line (Rho & Borkowski 2002).

One problem is position-to-position fluctuations of the cosmic X-ray background (CXB). We therefore estimated

the CXB flux assuming the photon index, the average surface brightness, and the Galactic absorption to be 1.412, 6.38×10^{-8} erg cm⁻² s⁻¹ sr⁻¹ (Kushino et al. 2002), and 1.4×10^{22} H cm⁻² (Dickey & Lockman 1990), respectively. Then the expected CXB level (the gray curve in figure 3) is only about 5% of the total background flux. Thus the error due to the CXB fluctuation can be neglected.

The major source of the background is the Galactic diffuse X-ray emission (GDXE) because W 28 is located near the Galactic plane and the Galactic center (GC). In fact, the Fe K α line at 6.7 keV seen in figure 3 is due to the GDXE. Since the surface brightness of the GDXE quickly decreases with the increasing distance from the Galactic plane with the scale height of $\lesssim 1^\circ$ (Uchiyama 2010¹), we selected the background region from the same Galactic latitude (figure 2 left) of W 28 (figure 2 right). The GDXE uncertainty is, therefore, due to the longitude distribution along the plane. The flux of the GDXE decreases as the distance from the GC increases with the scale length of $\sim 30^\circ$ (Uchiyama 2010). Then the GDXE on the background region is estimated to be about 5% smaller than that on W 28. Still we found no excess from W 28 above the background in the hard X-ray band, and hence no hard X-ray emission above 5 keV for W 28 is very conservative conclusion.

3.2. Spectrum

We subtracted the background spectrum (the red data in figure 3) from the source spectrum (the blue data in figure 3). The result is shown in figure 4. We can see many K-shell emission lines from highly ionized neon (Ne), magnesium (Mg), silicon (Si), and sulfur (S) as well as L-shell emission lines from Fe. We therefore examined several optically thin thermal plasma models. In the spectral analysis, we used the SPEX (Kaastra et al. 1996) software version 2.02.02. The redistribution matrix and the auxiliary response functions were generated by xisrmfgen and xissimarfgen (Ishisaki et al. 2007), respectively, with the latest rmfparam files version 20110708. The abundances for the absorption of interstellar medium (ISM: Morrison & McCammon 1983) were assumed to be one solar (Anders & Grevesse 1989), using the Absm model in SPEX. The abundances for Ne, Mg, Si, S, and Fe in the thermal plasma were free parameters, while those of oxygen (O), argon (Ar) and calcium (Ca), and nickel (Ni) were assumed to be the same as those of Ne, S, and Fe, respectively. The other elements, including carbon (C) and nitrogen (N) were fixed to one solar.

3.2.1. CIE Plasmas

We tried a single-temperature optically thin thermal plasma model in CIE (the Cie model in SPEX). The result is shown in figure 4a. Although we fit simultaneously for the FI and BI spectra, we show only the best-fit FI spectrum for simplicity. As is seen in figure 4a, this model obviously failed to reproduce the spectrum with $\chi^2/\text{d.o.f.}$ of 2160/641. We therefore examined a two-temperature CIE model (figure 4b), with coupled abundances for each

¹ Available at <http://repository.tksc.jaxa.jp/pl/dr/IS8000028000/en>

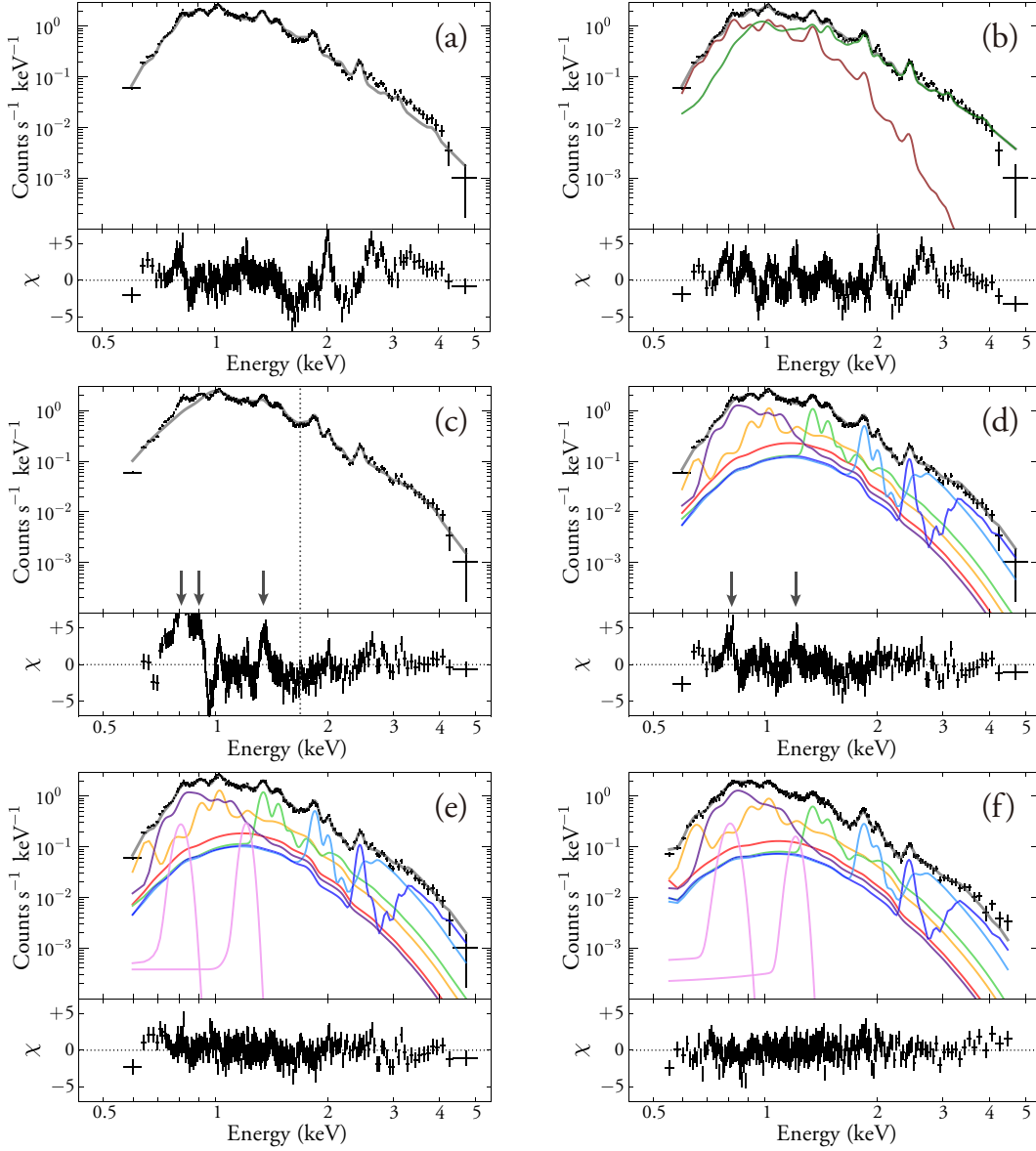


Fig. 4. Background-subtracted spectra (the black crosses) with the best-fit models. For visibility, only data and models for the merged FI are displayed except for (f). Each panel shows results of different models: (a) single-temperature CIE, (b) two-temperature CIE, (c) single- T_z recombining plasma model, (d) multi- T_z recombining plasma model, (e) the same as (d) but artificial Gaussians at 0.8 and 1.2 keV (pink) are added, and (f) the same as (e) but for BI. The thick gray curves are the total emission, while the thin colored curves are each component: low- kT component in dark red and high- kT component in dark green for (b); C and N in red, O and Ne in orange, Mg in light green, Si in light blue, S, Ar, and Ca in dark blue, Fe and Ni in purple for (d), (e), and (f). The solid arrows in (c) indicate the $K\alpha$ line centers of He-like Mg and Ne, and L-shell complex of Fe. The solid arrows in (d) are L-shell transitions of Fe.

element between the two CIE components. This model also failed to reproduce the spectrum with $\chi^2/\text{d.o.f.}$ of 1753/639. The best-fit parameters for these CIE models are given in table 2. In addition to the 0.77-keV plasma, W 28 requires 0.24-keV plasma instead of the 1.8-keV plasma of the ASCA results (Rho & Borkowski 2002). The authors proposed that W 28 is a peculiar MM SNR because of the presence of the high-temperature plasma of 1.8 keV. Our results of the 0.24+0.77-keV temperature plasma revised the interpretation of W 28 to be a typical MM SNR (0.4–0.9-keV temperature; Rho & Petre

1998). This revised picture comes from the absence of the high energy photons above ~ 5 keV in the Suzaku spectrum, which would be due to proper background subtraction (subsection 3.1). To improve the value of $\chi^2/\text{d.o.f.}$, we added further CIE components, but found no significant improvement. The most remarkable residuals in any CIE model are line-like excess at the Si Lyman α energy (2.0 keV) and bump-like structures at 2.4–5.0 keV.

3.2.2. Recombining Plasma Model with Single T_z

The bumps at 2.4–5.0 keV have two rising edges at 2.4 and 3.2 keV, which are most probably due to RRCs

Table 2. Best-fit parameters with CIE and single- T_z recombining plasma models.

Parameter	Single-temperature CIE	Two-temperature CIE	Single- T_z recombining plasma
N_H (10^{21} cm $^{-2}$)	$3.90^{+0.07}_{-0.07}$	$6.28^{+0.14}_{-0.15}$	$2.99^{+0.04}_{-0.03}$
VEM_1 (10^{56} cm $^{-3}$)*	$21.1^{+0.7}_{-0.6}$	103^{+13}_{-12}	$64.6^{+0.9}_{-0.9}$
VEM_2 (10^{56} cm $^{-3}$)*	...	$13.6^{+0.5}_{-0.5}$...
kT_1 (keV)	$0.62^{+0.01}_{-0.01}$	$0.24^{+0.01}_{-0.01}$...
kT_2 (keV)	...	$0.77^{+0.01}_{-0.01}$...
kT_e (keV)	0.43 (fixed)
kT_z (keV)	0.95 (fixed)
Abundance (solar)			
... Ne	$0.39^{+0.02}_{-0.02}$	$0.13^{+0.01}_{-0.01}$	≤ 0.01
... Mg	$0.36^{+0.02}_{-0.02}$	$0.41^{+0.02}_{-0.02}$	$0.18^{+0.01}_{-0.01}$
... Si	$0.25^{+0.01}_{-0.01}$	$0.32^{+0.02}_{-0.02}$	$0.20^{+0.01}_{-0.01}$
... S	$0.50^{+0.04}_{-0.04}$	$0.43^{+0.04}_{-0.03}$	$0.26^{+0.02}_{-0.02}$
... Fe	$0.14^{+0.01}_{-0.01}$	$0.23^{+0.01}_{-0.01}$	$0.06^{+0.01}_{-0.01}$
$\chi^2/\text{d.o.f.}$	2160/641	1753/639	6914/642

* Volume emission measure at the distance of 2 kpc: $VEM = \int n_e n_p dV$, where n_e , n_p , and V , are the electron and proton densities, and the emitting volume, respectively.

of He-like Si and S, respectively (Ohnishi et al. 2011). Together with the strong Si Lyman α residual, the spectrum is due to a recombining plasma, at least for Si and S. We thus tried a recombining plasma model in the RRC band of Si and S (1.7–5.0 keV). Then the residuals found in the 1.7–5.0 keV band disappear with the best-fit T_z of $0.95^{+0.01}_{-0.09}$ keV and T_e of $0.43^{+0.03}_{-0.01}$ keV. Fixing these best-fit temperatures, we made a full energy band fit. The free parameters were abundances of Ne, Mg, Si, S, and Fe, and N_H . The result is, however, unacceptable with $\chi^2/\text{d.o.f.}$ of 6914/642 (figure 4c). As shown by the solid arrows in figure 4c, remarkable excess are found at the K α lines of He-like Mg (1.35 keV) and Ne (0.92 keV) and the Fe L-shell complex at ~ 0.8 keV.

3.2.3. Multi- T_z Recombining Plasma

The data excess near the K α lines of He-like Mg and Ne indicates underestimation of the He-like line fluxes compared to the H-like line (see the solid arrows in figure 4c). This supports that T_z for Mg is significantly lower than those of Si and S. We therefore introduced a recombining plasma model with different T_z for each element (figure 4d). Since no spectral code to directly describe such a plasma is available, we approximated the model with the combination of several single- T_z plasmas whose T_e are coupled among the all plasmas. We grouped the elements into six sub-groups assuming the same abundances in each sub-group (see the caption of figure 4). For C and N, we fixed T_z to T_e .

As shown in figure 4d, this model (model A) well reproduced the overall structure of the observed spectrum. Still some residuals remain at ~ 0.8 and ~ 1.2 keV (see the solid arrows in figure 4d). These features are known to originate from incomplete atomic data in the current spectral code. The former comes from the uncertain intensity ratio of the Fe L-shell transitions of 3s \rightarrow 2p and 3d \rightarrow 2p (Gu et al. 2007 and reference therein). The present code may underestimate the 0.8 keV line flux. The latter is due to the

Table 3. Best-fit parameters with a multi- T_z recombining plasma model.

Parameter	A	B
N_H (10^{21} cm $^{-2}$)	$4.65^{+0.15}_{-0.12}$	$4.70^{+0.15}_{-0.11}$
VEM (10^{56} cm $^{-3}$)*	$60.7^{+9.3}_{-7.1}$	$47.1^{+7.3}_{-5.8}$
kT_e (keV)	$0.39^{+0.02}_{-0.02}$	$0.40^{+0.02}_{-0.03}$
kT_z (keV)		
... Ne	$0.48^{+0.04}_{-0.03}$	$0.46^{+0.05}_{-0.04}$
... Mg	$0.66^{+0.06}_{-0.05}$	$0.66^{+0.07}_{-0.06}$
... Si	$1.01^{+0.07}_{-0.06}$	$1.01^{+0.08}_{-0.08}$
... S	$0.95^{+0.11}_{-0.09}$	$0.96^{+0.14}_{-0.10}$
... Fe	$0.58^{+0.04}_{-0.04}$	$0.58^{+0.05}_{-0.05}$
Abundance (solar)		
... Ne	$0.16^{+0.01}_{-0.02}$	$0.23^{+0.03}_{-0.02}$
... Mg	$0.32^{+0.02}_{-0.02}$	$0.44^{+0.04}_{-0.03}$
... Si	$0.26^{+0.02}_{-0.03}$	$0.34^{+0.03}_{-0.04}$
... S	$0.33^{+0.08}_{-0.08}$	$0.40^{+0.09}_{-0.09}$
... Fe	$0.10^{+0.01}_{-0.01}$	$0.11^{+0.01}_{-0.01}$
$\chi^2/\text{d.o.f.}$	1268/636	893/634

* The value at the distance of 2 kpc.

lack of a number of the Fe L-shell lines by the transitions from highly excited states of $n \geq 5$ (Brickhouse et al. 2000). Thus, we artificially added two Gaussians at 0.8 keV and 1.2 keV (figure 4e and 4f). Then the fit largely improved (model B; $\chi^2/\text{d.o.f.} = 893/634$). The best-fit parameters for Model A and B are listed in table 3. We see that the best-fit T_z are essentially the same between model A and B. The best-fit T_z are different among elements with higher temperature than T_e (table 3).

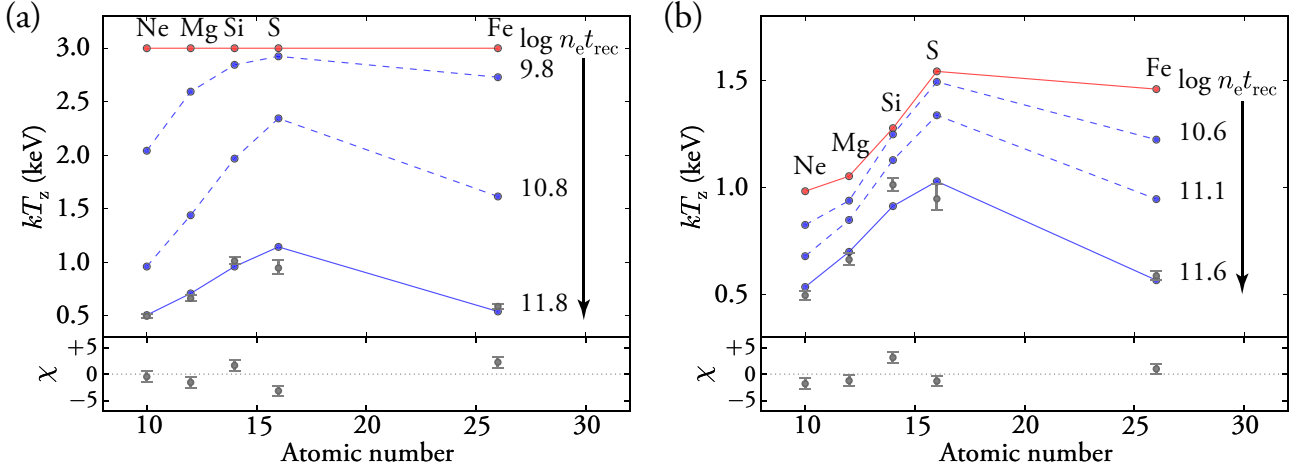


Fig. 5. Time evolution of T_z in recombining plasmas with the initial conditions of (a) $T_{z0} = 3.0$ keV for all elements, and (b) T_{z0} realized by an ionizing plasma with $T_e' = 10$ keV and $n_e t_{\text{ioni}} = 10^{11}$ s cm $^{-3}$. The gray circles with bars show the observed T_z with 1- σ statistical errors. The direction of evolution as a function of $n_e t_{\text{rec}}$ is indicated by the vertical arrows. The solid lines in red and blue respectively show the initial and final states, while the dashed blue lines show transitional states.

4. Discussion

We have found that the observed spectrum can be reproduced by a multi- T_z recombining plasma. The recombining plasmas in SNRs are not expected in the standard scenario, and hence there must be a missing branch of evolution of SNRs. Several ideas have been proposed, such as rapid electron cooling by adiabatic rarefaction (Itoh & Masai 1989), or conduction cooling by ambient cold matter (Kawasaki et al. 2002), extra-ionization by high-energy photons (Kawasaki et al. 2002) or by supra-thermal particles (Ohnishi et al. 2011), and so on. Any scenario may compose of two processes; (1) initial process to make a plasma of higher T_z than T_e , and (2) gradual relaxation of the recombining plasma toward CIE. We propose that the process (2) carries the essential roll to make element-dependent T_z . Based on the simulation of the T_z relaxation in time and comparison with the observed multi- T_z values, possible origin of the recombining plasma from W 28 is discussed in the following subsections.

4.1. Recombination Timescale

Difference of T_z among elements can appear in a relaxation epoch of recombining plasma to CIE because the relaxation timescale is different from element to element. Numerical studies have demonstrated that the relaxation timescale basically shows monotonic increase with atomic number, except for Fe and Ni (e.g., see figure 1 of Smith & Hughes 2010). These two heavy elements have shorter timescales than the other lighter elements at T_z from sub to a few keV, because the L-shell processes are dominant for Fe and Ni, while the K-shell processes are dominant for the others in this temperature range. The observed T_z values appear to satisfy this trend (table 3).

To examine whether the difference in recombination timescale can quantitatively explain the observed T_z , we simulate time evolutions of T_z in a recombining plasma

by using the Neij model in SPEX. The parameters are the initial ionization temperature T_{z0} , T_e , and the recombination time $n_e t_{\text{rec}}$, where n_e and t_{rec} are the density of electrons and the elapsed time, respectively.

We have tried many sets of (T_{z0}, t_{rec}) for fixed T_e of 0.4 keV following the best-fit value (table 3). We obtained similar best-fit T_z distribution from different parameter set of (T_{z0}, t_{rec}) . We therefore constrain the parameter set within physically reasonable values. One plausible case of $T_{z0} = 3$ keV is given in figure 5a, which shows the simulated decrease of T_z with time ($n_e t_{\text{rec}}$). We find the best-fit recombination time to be $n_e t_{\text{rec}} = 10^{11.8}$ s cm $^{-3}$. The simulated T_z values after $10^{11.8}$ s cm $^{-3}$, is close to the observation with $\chi^2/\text{d.o.f.}$ of $\sim 21/4$. We caution that the $\chi^2/\text{d.o.f.}$ value is just for reference to compare a more complex simulation given in the next subsection, and should not be taken seriously, because the major uncertainty of the observed T_z is not statistic error but systematic one due to incomplete modeling and/or atomic data in the analyses.

4.2. Initial Variation of T_z

In a more general case, initial T_{z0} should be different among elements. We hence simulate the time evolution of T_z in this case. The simulation consists of two steps. In the first step, we simulate the evolution of T_z in an ionizing plasma. This gives the element-dependent T_{z0} . Then using this result, we simulate a recombining plasma as was done in the previous subsection.

The parameters are the electron temperature during the ionizing phase T_e' , the ionization time $n_e t_{\text{ioni}}$, and the recombination time $n_e t_{\text{rec}}$. The electron temperatures during the two processes, T_e' and T_e , are assumed to be 10 keV and 0.4 keV, respectively.

In figure 5b, we plot decrease of T_z during the recombining phase for the case of $T_e' = 10$ keV and $n_e t_{\text{ioni}} = 10^{11.0}$ s cm $^{-3}$. This combined process gives a better fit

to the observed T_z , than that of the single relaxation process of recombining plasma (see subsection 4.1) at $n_e t_{\text{rec}} = 10^{11.6} \text{ s cm}^{-3}$ with $\chi^2/\text{d.o.f.}$ of $\sim 17/4$. One may argue that other combinations of the parameter values may also work as well. As we already noted, many combinations were examined and the recombination times are always found to be $\sim 10^{11.5} \text{ s cm}^{-3}$ or longer. Thus, the result of $n_e t_{\text{rec}}$ does not depend much on the initial conditions of T_{z0} .

4.3. Origin of Recombining Plasma in W 28

We have shown that the combination of the processes (1) and (2) provides a plausible scenario for producing the observed spectrum with the initial conditions given in figure 5(b) (see the beginning of Discussion and section 4.1). The initial conditions can be set by collisional ionization in thermal pool of electrons with no special ionization process such as photo-ionization or supra-thermal electrons. This supports the electron cooling scenario for W 28. In the simulation, $n_e t_{\text{rec}}$ is $\sim 10^{11.6}$, which corresponds to $\sim 10^4 \times (n_e/1 \text{ cm}^{-3})^{-1} \text{ yr}$, roughly consistent with the age of W 28. Thus, the recombination time is consistent with the rarefaction scenario (Itoh & Masai 1989).

This recombination time is also nearly the same order of the cooling timescale by thermal conduction, which is estimated to be $\sim 2 \times 10^4 \times (n_e/1 \text{ cm}^{-3}) \text{ yr}$ for the plasma of 6-pc diameter (see equation 5 in Kawasaki et al. 2002). However, we found no spatial correlation of the recombining plasma to the molecular clouds (Sawada et al. 2012, in preparation), which may not favor the thermal conduction scenario. We therefore propose the rarefaction scenario (Itoh & Masai 1989), and discuss along this scenario in the following paragraphs. More quantitative comparison of these two models will be given in the next paper using the results of spatial distribution of the recombining plasma (Sawada et al. 2012, in preparation).

The initial event of the rarefaction scenario would be a type-II supernova explosion in dense circum-stellar medium (CSM) made by stellar winds from the massive progenitor. Assuming a spherical plasma with the diameter of 6 pc, the mass of the X-ray emitting gas in the center region is estimated to be $\sim 5 M_\odot$. This value is similar to that of a massive progenitor, and hence provides further circumstantial support for the rarefaction scenario. The shock-heated ejecta and CSM experience rapid electron cooling due to adiabatic expansion after shock break-out to the rarefied ambient ISM. The break-out and hence the cooling, occur at the early phase of the SNR evolution (about several 10–100 yr after the explosion; Itoh & Masai 1989). Thus most of the life would be in the relaxation phase of the recombining plasma, consistent with the large $n_e t_{\text{rec}}$ values obtained in our simulations. Due to the dense environment of CSM, the shocked gas quickly reaches a temperature of several keV before the break-out, in good agreement with the T_{z0} values assumed in our simulations.

Shimizu, Masai, & Koyama (2011) extended the previous calculation of Itoh & Masai (1989) to non-symmetric cases and found that center-filled X-ray morphologies are

realized with anisotropic CSM due to the rotation of a progenitor star. The size of the X-ray emitting plasma is about a few 10 pc, which is consistent with that of W 28. Therefore, this scenario can explain both the spectral and spatial structures of the X-ray emission from W 28.

The authors thank K. Masai, T. Shimizu, and H. Yamaguchi for valuable discussion, J. Kaastra and J. de Plaa for their useful comments on spectral modeling, and S. Nakashima, M. Nobukawa, H. Uchida, and H. Uchiyama for improving the draft. We also thank all of the Suzaku team members for their full support of the Suzaku project. We acknowledge the financial support from the Ministry of Education, Culture, Sports, Science and Technology (MEXT) of Japan; the Grant-in-Aid for the Global COE Program “The Next Generation of Physics, Spun from Universality and Emergence” and others for Scientific Research B (No. 20340043 and 23340047). MS is supported by Japan Society for the Promotion of Science (JSPS) Research Fellowship for Young Scientists. KK is supported by the Challenging Exploratory Research program.

References

- Abdo, A. A., et al. 2010a, *ApJ*, 712, 459
- Abdo, A. A., et al. 2010b, *ApJ*, 718, 348
- Aharonian, F., et al. 2008, *A&A*, 481, 401
- Anders, E., & Grevesse, N. 1989, *Geochim. Cosmochim. Acta*, 53, 197
- Arikawa, Y., Tatematsu, K., Sekimoto, Y., & Takahashi, T. 1999, *PASJ*, 51, L7
- Bautz, M. W., Kissel, S. E., Prigozhin, G. Y., LaMarr, B., Burke, B. E., & Gregory, J. A. 2004, *Proc. SPIE*, 5501, 111
- Brickhouse, N. S., Dupree, A. K., Edgar, R. J., Liedahl, D. A., Drake, S. A., White, N. E., & Singh, K. P. 2000, *ApJ*, 530, 387
- Dickey, J. M., & Lockman, F. J. 1990, *ARA&A*, 28, 215
- Dubner, G. M., Velázquez, P. F., Goss, W. M., & Holdaway, M. A. 2000, *AJ*, 120, 1933
- Gu, M. F., Chen, H., Brown, G. V., Beiersdorfer, P., & Kahn, S. M. 2007, *ApJ*, 670, 1504
- Ishisaki, Y., et al. 2007, *PASJ*, 59, S113
- Itoh, H., & Masai, K. 1989, *MNRAS*, 236, 885
- Kaastra, J. S., Mewe, R., & Nieuwenhuijzen, H. 1996, *UV and X-ray Spectroscopy of Astrophysical and Laboratory Plasmas*, 411
- Kaspi, V. M., Lyne, A. G., Manchester, R. N., Johnston, S., D’Amico, N., & Shemar, S. L. 1993, *ApJL*, 409, L57
- Kawasaki, M. T., Ozaki, M., Nagase, F., Masai, K., Ishida, M., & Petre, R. 2002, *ApJ*, 572, 897
- Kinugasa, K., & Tsunemi, H. 1999, *PASJ*, 51, 239
- Koyama, K., et al. 2007, *PASJ*, 59, S23
- Kushino, A., Ishisaki, Y., Morita, U., Yamasaki, N. Y., Ishida, M., Ohashi, T., & Ueda, Y. 2002, *PASJ*, 54, 327
- Masai, K. 1984, *Ap&SS*, 98, 367
- Mitsuda, K., et al. 2007, *PASJ*, 59, S1
- Morrison, R., & McCammon, D. 1983, *ApJ*, 270, 119
- Ohnishi, T., Koyama, K., Tsuru, T. G., Masai, K., Yamaguchi, H., & Ozawa, M. 2011, *PASJ*, 63, 527
- Ozawa, M., Koyama, K., Yamaguchi, H., Masai, K., & Tamagawa, T. 2009, *ApJ*, 706, L71

- Reach, W. T., Rho, J., & Jarrett, T. H. 2005, *ApJ*, 618, 297
- Rho, J., & Borkowski, K. J. 2002, *ApJ*, 575, 201
- Rho, J., & Petre, R. 1998, *ApJ*, 503, L167
- Serlemitsos, P. J., et al. 2007, *PASJ*, 59, S9
- Shimizu, T., Masai, K., & Koyama, K. 2012, *PASJ*, 64, accepted.
- Smith, R. K., & Hughes, J. P. 2010, *ApJ*, 718, 583
- Snowden, S. L., et al. 1995, *ApJ*, 454, 643
- Tawa, N., et al. 2008, *PASJ*, 60, S11
- Uchiyama, H., et al. 2009, *PASJ*, 61, S9
- Uchiyama, H. 2010, Ph.D. Thesis, Kyoto University
- Uchiyama, H., Nobukawa, M., Tsuru, T. G., Koyama, K., & Matsumoto, H. 2011, *PASJ*, 63, S903.
- Velázquez, P. F., Dubner, G. M., Goss, W. M., & Green, A. J. 2002, *AJ*, 124, 2145
- Yamaguchi, H., Ozawa, M., Koyama, K., Masai, K., Hiraga, J. S., Ozaki, M., & Yonetoku, D. 2009, *ApJ*, 705, L6
- Yusef-Zadeh, F., Wardle, M., Rho, J., & Sakano, M. 2003a, *ApJ*, 585, 319
- Yusef-Zadeh, F., Wardle, M., & Roberts, D. A. 2003b, *ApJ*, 583, 267